



A thermodynamic and kinetic study of the formation and evolution of corrosion product scales on 13Cr stainless steel in a geothermal environment

Xiaoqi Yue^{a,b}, Lei Zhang^a, Chong Sun^c, Shusheng Xu^b, Chun Wang^b, Minxu Lu^a, Anne Neville^b, Yong Hua^{b,*}

^a Institute of Advanced Materials and Technology, University of Science and Technology Beijing, 30 Xueyuan Road, Beijing, 100083, China

^b Institute of Functional Surfaces, School of Mechanical Engineering, University of Leeds, Leeds, LS2 9JT, United Kingdom

^c Department of Chemical and Materials Engineering, University of Alberta, Edmonton, Alberta, T6G 1H9, Canada

ARTICLE INFO

Keywords:

13Cr stainless steel
FIBs
Thermodynamic
Film evolution

ABSTRACT

The formation and evolution of corrosion product scales on 13Cr stainless steel at 200 °C and various CO₂ partial pressures were investigated. Scanning electron microscope was used to show the physical nature of the scales formed at 0.27 MPa CO₂. The thin non-uniform layer was identified as FeCr₂O₄ by Raman Spectroscopy with a thick Cr(OH)₃ layer being determined at 2.85 MPa CO₂. These results provide a guide to understanding the mechanisms of CO₂ corrosion for 13Cr stainless steel exposed to high temperature and pressure and demonstrate the influence of thermodynamics and kinetics on the formation and evolution of the corrosion products.

1. Introduction

Stainless steels (SS), because of the passive films that form on their surface, have enhanced corrosion resistance due to passivation. They can resist environmental degradation and the passive film broadens the applications ranging from daily necessities to components of nuclear reactors [1,2]. Martensitic SSs are widely used in engineering components because of their excellent mechanical properties [3–6]. In recent years, the applications in arduous conditions of high temperature oil and gas well or in geothermal environments have attracted increased attention [7–10]. 13Cr SS has been commonly used in construction tubing materials based on cost-driven considerations and the ease of manufacture for those downhole applications [11–14].

The conventional 13Cr martensitic SS as a downhole tubing material was developed in the 1960s and the key gaps in the understanding that still exist relate to the corrosion behaviour of this material exposed to CO₂ environments at high temperature and high pressure (HTHP). Understanding the 13Cr martensitic SS corrosion at elevated temperatures up to 130 °C oil well conditions still remains an issue due to the complicated corrosion processes at the material interface [15]. In February 2019, a natural gas resource of more than 1000 billion cubic metres in Bohai sea at a depth of 4000 m at temperatures of around 200 °C was discovered. It has brought a renewed urgency to systematically study the corrosion behaviour of the pipeline materials subjected to such high temperature and high CO₂ pressure conditions [16,17].

A number of researchers studied the corrosion behaviour of alloy tubing materials exposed to HTHP environments [18–21]. In 1985, Ikeda et al. [21] studied the corrosion behaviour of 13Cr exposed to the temperature range between 30 °C and 250 °C and p_{CO_2} of 0.1 MPa and 3 MPa. They reported that the p_{CO_2} accelerated the corrosion rate of 13Cr SS at temperatures beyond 150 °C. This research provides an important reference for the application of 13Cr SS in ultra-deep wells. However, their study highlighted the limited information on the corrosion scale properties. Pfennig et al. [22] illustrated that the pit formation at 60 °C is driven by the formation of carbonic acid and the existence of HCO₃⁻ species. The CO₂ dissolved in the formation water to form H₂CO₃, and ionized to HCO₃⁻ and CO₃²⁻. The H₂CO₃ was a weak acid, which can corrode the pipeline materials [13,23]. Crolet et al. [24] found that HCO₃⁻ was produced by the cathodic reduction of CO₂ and resulted in an increase of pH value. It has been reported that the formation of the corrosion scales at high pressure played an important role in the improved corrosion resistance of 13Cr SS. They reported that the corrosion rate obtained at 10 MPa after 240-h immersion tests is lower than at ambient pressure due to the formation of the corrosion products on the surface [22]. In the absence of the corrosion products, the increase in CO₂ partial pressure (p_{CO_2}) resulted in an increase in the corrosion rates [25]. Mu et al. [26] studied the formation of corrosion products on 13Cr SS up to 90 °C by immersion of samples for 168 h. The results indicated that the films comprised an inner chromium oxide layer and an outer hydroxide/iron oxide layer, in which the high temperature damaged

* Corresponding author.

E-mail address: Y.Hua@leeds.ac.uk (Y. Hua).

<https://doi.org/10.1016/j.corsci.2020.108640>

Received 9 November 2019; Received in revised form 2 March 2020; Accepted 25 March 2020

Available online 01 April 2020

0010-938X/ © 2020 The Authors. Published by Elsevier Ltd. This is an open access article under the CC BY-NC-ND license

(<http://creativecommons.org/licenses/by-nc-nd/4.0/>).

Table 1
Chemical composition for 13Cr SS.

C	Si	Mn	P	S	Cr	Mo	Ni	Fe
0.15	0.36	0.56	0.006	0.008	13.5	–	0.02	Balance

the outer hydroxides and iron oxides in the stratum water. As the temperature or pressure is increased, it is widely accepted that the properties of the corrosion product films formed on the surface affect the metal corrosion resistance [27,28]. Zhang et al. [29] concluded that the increase in temperature results in the change of the composition of the corrosion product films formed on the 13Cr SS surface. Their results indicate that the corrosion product films contain both Cr_2O_3 and FeCO_3 for samples exposed to 150 °C and p_{CO_2} of 0.1 MPa. In recent work by Zhao et al. [30,31,46], both the electrochemical and mechanical properties of the corrosion product films on 13Cr SS up to 180 °C were characterised. Their results indicated that the changes in microstructure and composition lead to corrosion product films that were easier to be broken down and which had a higher pitting susceptibility, especially when the temperature was extended beyond 150 °C.

The temperature has been considered as one of the key factors for the safe application of 13Cr SS in high temperature oil and gas well or geothermal environments. However, the understanding of the influence of the p_{CO_2} on the formation of the corrosion product mechanisms in high-temperature conditions (such as at 200 °C) has received less attention. The purpose of the research is first to understand the capabilities of 13Cr SS steels in terms of corrosion resistance, the corrosion product formation mechanism as well as the protective properties of the corrosion product scales at elevated p_{CO_2} for downhole/geothermal applications. The role that p_{CO_2} plays in influencing the formation of corrosion product kinetics and the correlation with Pourbaix diagram assessments are needed to provide a complete understanding.

2. Experimental

2.1. Material and methods

The tested 13Cr SS (UNS S41000) specimens were 6 mm thick and 25 mm in diameter with a 3 mm hole. The elemental composition of 13Cr SS is listed in Table 1. The sample preparation has been provided in our previous publication [8]. Samples were kept in a desiccator for 1 day and an electronic balance within an accuracy of 10^{-5} g (W_0) was used before being put inside the autoclave. Fig. 1 exhibits the HTHP system for mass loss tests. All tests were performed placing two parallel samples and keep the volume to surface ratio at approximately 30 mL/cm².

The composition of the brine solution used in all experiments is

shown in Table 2. The brine solution was de-aerated by saturating with CO_2 in a separate container for at least 4 h per litre solution prior to testing. The autoclave and connected lines were purged with high-pressure CO_2 . After transferring the solution to the autoclave, the autoclave was then pressurized to the desired pressure and heated to 200 °C. The immersion time started when the autoclave reached 200 °C and ended before cooling. Normally, the heating time is about 40 min, while the cooling time was controlled within 10 min. Table 2 and Table 3 show all the test conditions, the calculated pH values at various p_{CO_2} and 200 °C by using OLI Stream [32].

The samples were removed from the autoclave, dried and weighed (W_1). The removal of the corrosion products was used Clark's solution according to the ASTM G1-03 standard (Designation C.3.1) [33]. Weighed again of the samples without the corrosion products to have the final weight (W_2). The total mass loss of the samples was obtained via Eq. (1).

$$W = W_0 - W_2 \quad (1)$$

The obtained mass loss value via Eq. (1) was used to calculate the corrosion rate (C_R) via Eq. (2).

$$C_R = \frac{87600W}{t\rho A} \quad (2)$$

Where C_R is the corrosion rate, mm/year; A is exposed surface area in cm²; ρ is steel density, g/cm³, and t represents the immersion time, hrs.

2.2. Surface characterisation of the corrosion product scales

The surface morphologies and their cross-sectional morphologies of the corrosion products were observed by SEM at an accelerating voltage of 20 kV via secondary electron (SE) and Focused ion beam scanning electron microscope (FIB-SEM) at 10 kV via Back-Scattered Electron (BSE) respectively. The crystalline corrosion products were characterised by X-Ray Diffraction (XRD) using a Cu K α radiation with an active area of 10 mm × 10 mm, a range of $2\theta = 20\text{--}80^\circ$ and a step size of 0.033 per second. Raman spectroscopy (488 nm radiation) with an Ar ion laser was used to identify oxide species and EDS was used to detect the elemental compositions. X-Ray Photoelectron Spectroscopy (XPS) with a monochromatic X-ray source (a Al K α electrode at 15 kV and 150 W) was used to analyse the corrosion products at the very near surface of around 10 nm.

2.3. Corrosion simulation

OLI Analyzer Studio 3.1 was used to calculate the pH and Pourbaix diagrams which are relevant to the immersion tests. The single point calculation was employed using custom type. Accordingly, the total inflow was fixed considering that the brine was not renewed in the

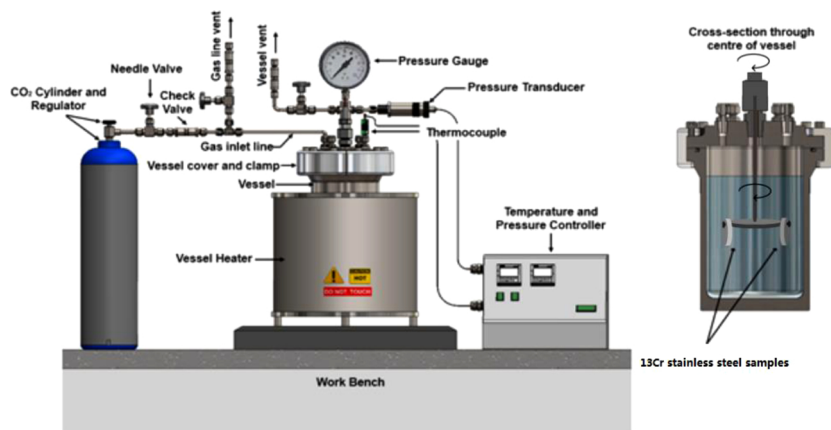


Fig. 1. HTHP autoclave system and the position of the samples in the autoclave [16].

Table 2
Experimental matrix at various p_{CO_2} at 200 °C.

Brine (mg/L)	Temp/°C	p_{CO_2} at 25 °C/ MPa	Calculated pH	p_{CO_2} / MPa	Total pressure/ MPa	Immersion time/hrs
NaCl solution, Cl ⁻ : 29503,HCO ₃ ⁻ : 585,	200	0.1	6.54	0.27	1.8	48
		0.3	6.25	0.65	2.2	
		1.0	5.86	1.54	3.1	
		2.0	5.55	2.85	4.5	

Table 3
Experimental matrix for various immersion times.

Brine (mg/L)	Temp °C	p_{CO_2} at 25 °C/ MPa	Calculated pH	p_{CO_2} / MPa	Total pressure/ MPa	Immersion time/hrs		
NaCl solution, Cl ⁻ : 29503,HCO ₃ ⁻ : 585,	200	0.1	6.54	0.27	1.8	5		
						48		
		2.0	5.55	2.85	4.5	120		
						5		
								48
								120

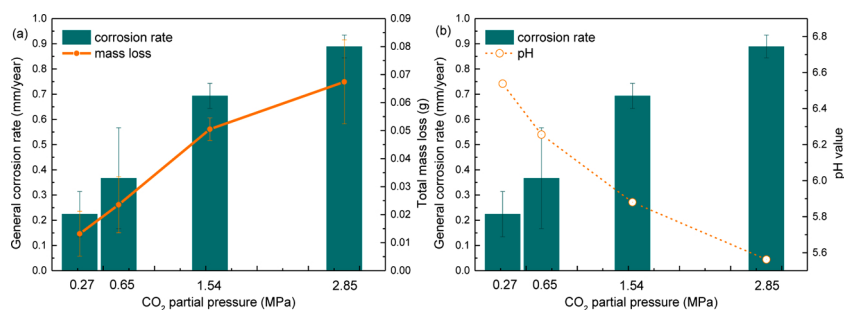


Fig. 2. (a) Corrosion rates and total mass loss of 13Cr SS, and (b) corresponding bulk pH at a constant temperature of 200°C and various p_{CO_2} values for 48 h.

laboratory conditions. The stability diagram was calculated using potential vs. pH type with a matrix of 88 %Fe and 12 %Cr.

3. Results

3.1. The effect of p_{CO_2} on the corrosion behaviour of 13Cr SS at 200°C for 48 h

Fig. 2 shows the corrosion rates, total mass loss of 13Cr SS, and corresponding bulk pH after 48 h immersion under various p_{CO_2} of 0.27 MPa, 0.65 MPa, 1.54 MPa, and 2.85 MPa at 200 °C. The pH values shown in Fig. 2b decreased with the increasing p_{CO_2} as expected. The results indicate that the highest corrosion rate was recorded at the highest p_{CO_2} of 2.85 MPa as expected. The general corrosion rates decreased from 0.889 mm/y to 0.224 mm/y when the p_{CO_2} reduced from 2.85 MPa to 0.27 MPa. It can be noted that the general corrosion rates increased significantly with the p_{CO_2} in conjunction with an increase in corrosion product mass. The results are aligned with Ikea et al. [25], who performed tests at 250 °C and p_{CO_2} of 0.1 MPa and 3.0 MPa on 13Cr SS over immersion time of 96 h. They recorded that the general corrosion rates increased from 0.3 mm/year at p_{CO_2} of 0.1 MPa to 2.5 mm/year at p_{CO_2} of 3.0 MPa.

The top-view SEM images of the 13Cr SS samples immersed in the solution at various p_{CO_2} are provided in Fig. 3. The steel surfaces appeared to be locally covered by crystalline corrosion products and the crystals were larger and increased in number with increasing p_{CO_2} .

Fig. 4 shows the cross-sectional SEM images of the 13Cr SS samples immersed in the solution after 48 h of exposure time under various p_{CO_2} environments. The 13Cr SS surface was covered by a thin inner corrosion product layer of 2 µm in thickness at p_{CO_2} of 0.27 MPa. As the p_{CO_2} was increased from 0.27 MPa to 2.85 MPa at 200 °C, the inner layer was

significantly thickened and reached almost 10 µm after 48 h of exposure.

In order to identify the nature of the corrosion product layers and the scattered crystals, XRD and Raman were employed. In Fig. 5, it is clear that only crystalline phases of FeCO_3 were identified on the surface. It can be noted that no Cr-containing corrosion products were detected by using XRD measurements and this suggests that the inner corrosion product layer was mainly an amorphous or nanoparticle layer which XRD cannot detect.

To complement the XRD results, Fig. 6 exhibits the constructed local Raman scans for the formation of the corrosion products on the 13Cr SS surface. The Raman spectra for the sample exposed to the p_{CO_2} of 0.27 MPa indicates a broad peak, which is located at 695 cm^{-1} and is representative of FeCr_2O_4 [34].

The peaks associated with the p_{CO_2} of 0.65 MPa shows the enhancement of the main peak located at 695 cm^{-1} . The spectra from the sample at 1.54 MPa indicates the main peak to be shifted to 717 cm^{-1} , corresponding to $\text{Cr}(\text{OH})_3$ [35]. As the p_{CO_2} increased to 2.85 MPa, the observed peak at 717 cm^{-1} becomes more clear and indicates the corrosion product is related to the enrichment of $\text{Cr}(\text{OH})_3$. These observations prove that the formation of various corrosion products takes place on the 13Cr SS surface as the p_{CO_2} is increased.

3.2. The formation of corrosion product scales on 13Cr SS at 0.27 MPa p_{CO_2} at 200°C

To understand the different formation processes of the corrosion product layers developed on the surface, as well as their protective capabilities under various p_{CO_2} , two p_{CO_2} of 0.27 MPa and 2.85 MPa were selected.

Fig. 7a exhibits the corrosion product mass and the general

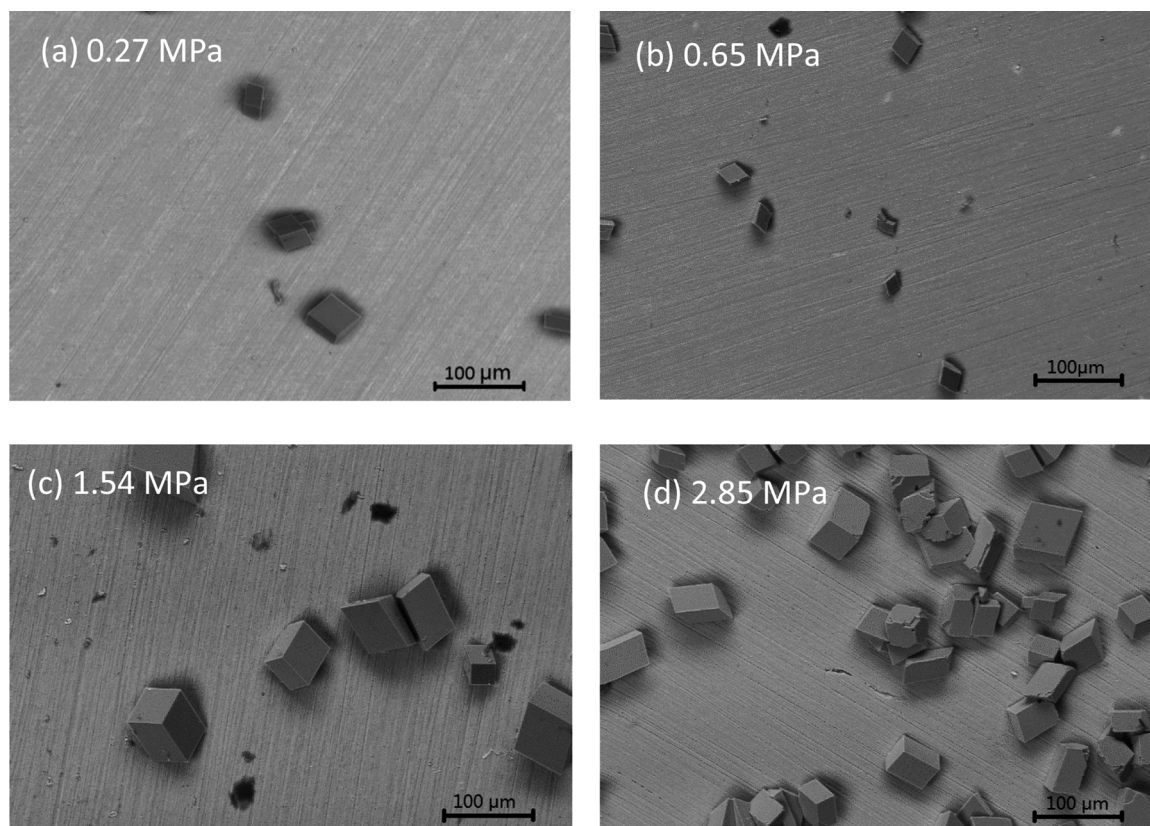


Fig. 3. Top-view SEM images of 13Cr SS immersed in the solution at a constant temperature of 200°C and (a) 0.27 MPa, (b) 0.65 MPa, (c) 1.54 MPa, and (d) 2.85 MPa of p_{CO_2} for 48 h.

corrosion rates of 13Cr SS samples immersed in the solution under various immersion times of 5, 48 and 120 h at 200 °C and low p_{CO_2} of 0.27 MPa. Fig. 7a indicates that the general corrosion rates decreased as a function of time and suggests that the formation of the corrosion product layer has excellent protection in this condition. Interestingly, the corrosion product mass remained almost unchanged from 48 to 120 h, suggesting that the observed protective and dense inner layer on the surface can block the active sites on the surface and has the ability to act as a diffusion barrier to protect the surface from further corrosion attack [8,34]. Besides, the predicted bulk pH at various immersion times is shown in Fig. 7b. It can be seen that the bulk pH increased slightly (less than 0.012) over 120 h and suggest that the rate of dissolution for 13Cr exposed to 0.27 MPa p_{CO_2} is slow.

Fig. 8 indicates the top-view SEM images of 13Cr SS exposed to the solution at 200 °C and 0.27 MPa of p_{CO_2} after different immersion times. There are no visible FeCO_3 crystals distributed on the surface in the first 5 h. The crystals appeared on the surface after 48 h of exposure time (Fig. 8(b)) and the larger cubic crystals were clearly precipitated on the surface after 120 h as shown in Fig. 8(c). As the exposure duration time is increased, the number of the crystalline FeCO_3 does not significantly increase, whereas the size of the FeCO_3 crystals increases via the SEM images.

To further determine the nature of the corrosion products formed at various immersion times, XRD was employed. Only crystalline FeCO_3 was detected for samples exposed to the solution after 48 h. The peaks of FeCO_3 crystals were limited to some predominant crystal orientations, though the intensity of these peaks, especially the peak for (104), increased with time as shown in Fig. 9. For the identification of the inner corrosion product layer, Raman data was used, and the results are shown in Fig. 10. The inner layer is identified to be FeCr_2O_4 and remained unchanged with time. The intensity of FeCr_2O_4 increased with time, suggesting the thickness of the FeCr_2O_4 layer increased.

To completely detect all the amorphous and crystalline phases on the 13Cr SS surface, XPS was employed. The fitting curves of the Fe 2p3/2 peaks confirm the peaks at 710.5 eV and 712 eV are FeCr_2O_4 [36] and FeCO_3 [37]. The Cr 2p3/2 peaks are located at 576.7 eV, 577.2 eV, and 578.3 eV corresponding to Cr_2O_3 , $\text{Cr}(\text{OH})_3$, and FeCr_2O_4 [37,38]. Meanwhile, fitting of the peak binding energies verified that O was present as O^{2-} , OH^- , along with CO_3^{2-} at 530.5 eV, 533.3 eV and 532.5 eV, respectively [39]. The results in Fig. 11 indicate the corrosion products are mainly FeCr_2O_4 , Cr_2O_3 , $\text{Cr}(\text{OH})_3$, and FeCO_3 for 0.27 MPa of p_{CO_2} .

To confirm the elemental composition and the thickness of the inner corrosion layer, cross-sections were prepared using FIB. Fig. 12(a and b) exhibits the corrosion product is approximately 150 nm in thickness after 5 h. The corrosion products in Fig. 12 indicate that the double-layered structure comprising of an inner FeCr_2O_4 layer and the outer FeCO_3 layer after 120 h of exposure. The inner corrosion layer appears to be non-uniform, approximately between 0.5 and 3 μm. Referring to the low general corrosion rate (less than 0.1 mm/year after 120 h exposure) as shown in Fig. 7, the formation of the inner layer in a 0.27 MPa CO_2 condition provides better corrosion resistance than that in the p_{CO_2} of 2.85 MPa under the test condition here. From the EDS line scan analyses as shown in Fig. 13, the inner layer contains a high concentration of oxygen, iron, and chromium.

3.3. The formation of corrosion product scales on 13Cr SS at p_{CO_2} of 2.85 MPa and 200°C

Fig. 14 shows the corrosion product mass, the general corrosion rates of the samples, and the predicted solution pH at 200 °C and p_{CO_2} of 2.85 MPa for various immersion times. It shows that the general corrosion rate was high at 3.5 mm/year after the first 5 h and was due to the selective dissolution of the metal ions (Fe^{2+} and Cr^{3+}) within the

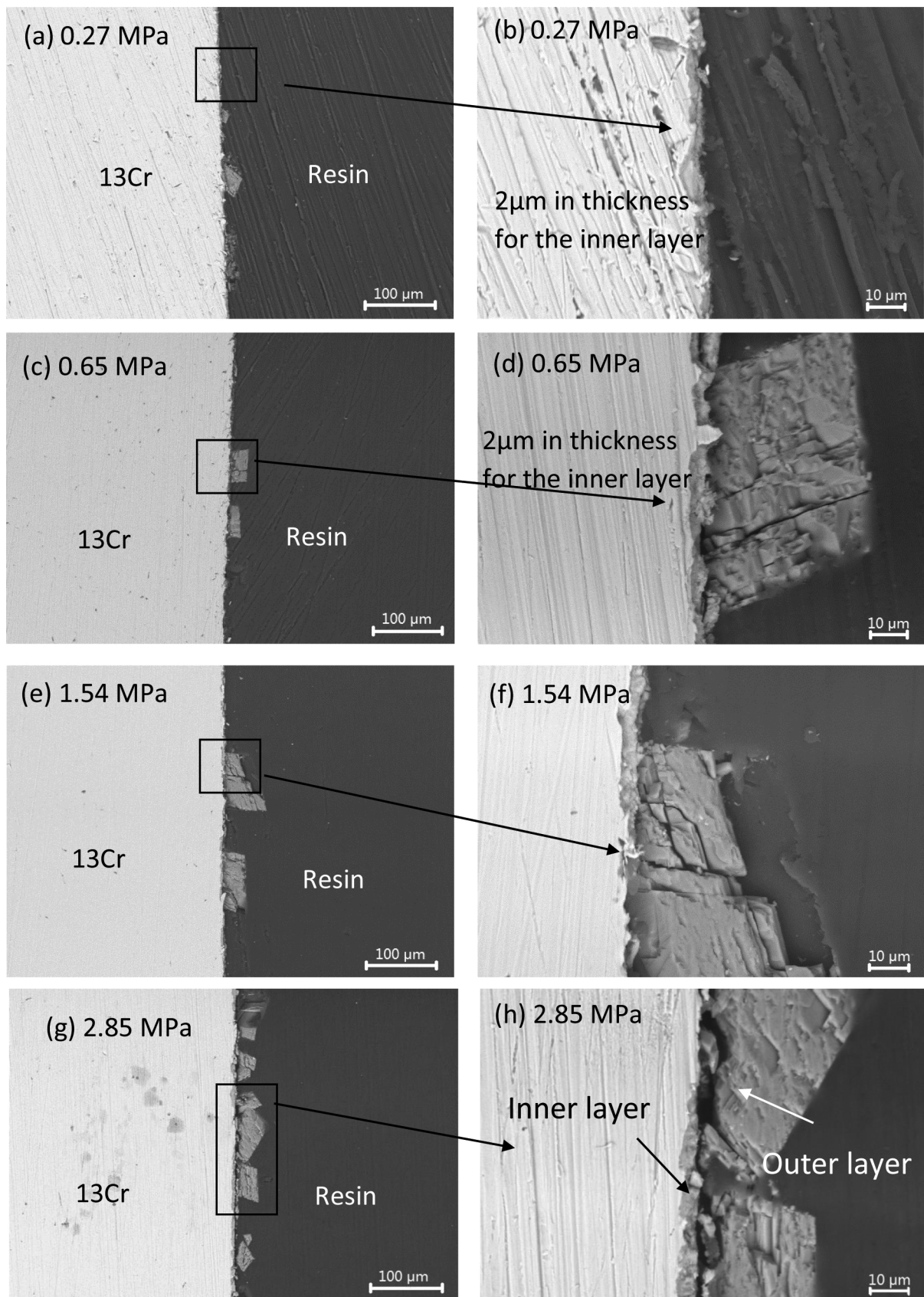


Fig. 4. Cross-sectional SEM images of 13Cr SS immersed in the solution at a constant temperature of 200°C and (a) (b) 0.27 MPa, (c) (d) 0.65 MPa, (e) (f) 1.54 MPa, and (g) (h) 2.85 MPa of p_{CO_2} for 48 h.

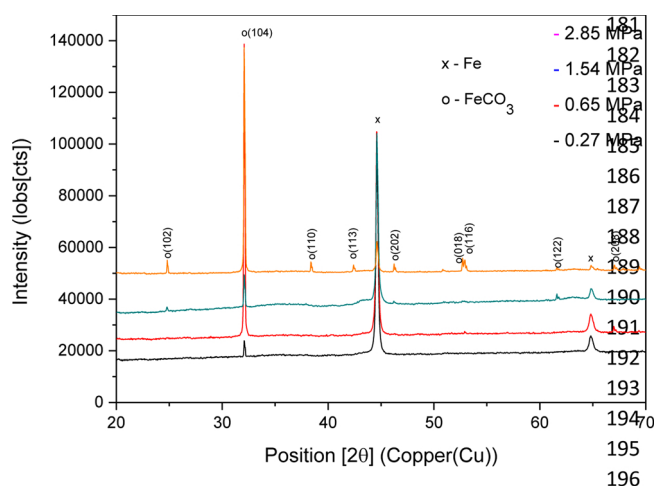


Fig. 5. Overall XRD analysis of the 13Cr SS samples exposed to the solution at 200 °C and various p_{CO_2} for 48 h.

steel [25]. The corrosion rate reduced over the test duration and reached a final corrosion rate of 0.8 mm/year after 120 h of exposure. The corrosion rate results at high p_{CO_2} of 2.85 MPa point out that it is the same trend to the results at 0.27 MPa. However, the corrosion product mass increases linearly whereas, in 0.27 MPa it reaches a plateau after 120 h of exposure. The corrosion rates reduced due to the corrosion product scales formed on the 13Cr SS surface (Fig. 15). Fig. 15a indicates that the corrosion product scales began to precipitate on the 13Cr SS surface after 5 h and covered almost the entire surface after 120 h. It is interesting to note that an inner layer was observed as shown in Fig. 15 (c) and (d) on the surface. For all the immersion periods, the results indicated that the increase in bulk pH was approximately 0.05 over 120 h, and is higher than the 0.012 for the low p_{CO_2} of 0.27 MPa as shown in Fig. 7. These results suggest that the solution is more corrosive and the rate of dissolution for 13Cr exposed to 2.85 MPa is faster than that of at low p_{CO_2} .

The XRD measurements were conducted for the samples exposed to the solution at different immersion times as shown in Fig. 16. The observed large cubic crystals are confirmed as FeCO_3 . The layer beneath the FeCO_3 crystals cannot be detected, suggesting that the layer is amorphous in nature and/or too thin.

The Raman spectra (Fig. 17) for the regions without a covering of FeCO_3 crystals shows a main peak located at 717 cm^{-1} was confirmed as the amorphous phase of $\text{Cr}(\text{OH})_3$. As can be noticed, the spectrum at 5 h also has a bump at 695 cm^{-1} , which indicates the presence of FeCr_2O_4 . It is the $\text{Cr}(\text{OH})_3$ layer that appears to be largely responsible

for the stable corrosion rates of 13Cr SS under higher p_{CO_2} as shown in Fig. 14.

The use of XPS is to determine the potential corrosion products which XRD and Raman cannot detect on the surface. As shown in Fig. 18, the $\text{Fe}2p_{3/2}$ scan for 13Cr confirms the peaks at 710.5 and 712 eV are FeCr_2O_4 [36] and FeCO_3 [37], respectively. The $\text{Cr} 2p_{3/2}$ peaks are located at 576.7 eV, 577.2 eV, and 578.3 eV corresponding to Cr_2O_3 , $\text{Cr}(\text{OH})_3$, and FeCr_2O_4 [37,38]. Fitting of the peak binding energies verified that O was present as oxides, hydroxide, along with carbonate at 530.5 eV, 533.3 eV, and 532.5 eV, respectively [39]. Therefore, the corrosion products detected on the surface of 13Cr at 2.85 MPa p_{CO_2} are mainly FeCO_3 , $\text{Cr}(\text{OH})_3$ and Cr_2O_3 . It is interesting to note that a small amount FeCr_2O_4 was observed for the higher p_{CO_2} (Fig. 18) in comparison to that of the low p_{CO_2} in Fig. 11.

To complement the XRD, Raman and XPS results, FIBS/EDX was also used to further analyse the corrosion products in terms of the thickness and elemental composition. The samples exposed to 200 °C and 2.85 MPa p_{CO_2} after 5 and 120 h were selected and taken for Focused Ion Beam (FIB) sample preparation. Two test samples covered by corrosion products were selected for analysis as shown in Fig. 19. Fig. 19(a and b) illustrates that the inner layer below the FeCO_3 crystals was approximately 0.2 μm in thickness after 5 h. The corrosion products also display the double-layered structure comprising of inner and outer layers after 120 h of exposure. A uniform inner layer was observed, and it covered the entire surface. Fig. 19(c) shows that the thickness of the inner layer was uniform across the steel surface and the thickness of the inner layer is approximately 10 μm . These observations are also supported by the EDX line scans provided in Fig. 20(a) and (b). From the EDX line scan analyses shown in Fig. 20, the inner layer contains a high concentration of oxygen and the chromium content becomes more significant especially after 120 h of exposure.

4. Discussion

4.1. The predicted corrosion products under high temperature and pressure CO_2 environments

Fig. 21 shows the constructed Pourbaix diagrams by using OLI software [32] at 200 °C and 0.27 or 2.85 MPa p_{CO_2} for the Fe-Cr- CO_2 - H_2O system, respectively. Fig. 21 shows the constructed Pourbaix diagrams for the formation of thermodynamically stable corrosion products on the 13Cr SS surface at both p_{CO_2} corresponding to the corrosion reactions at the early stage. Considering the locations of the two markers in Fig. 21 (the initial pH is 6.53 and initial corrosion potential is -0.51 V/SHE in the system), it is clear that the local pH is near the point within the regions where FeCr_2O_4 , Cr_2O_3 , and $\text{Cr}(\text{OH})_3$ are thermodynamically stable for a low p_{CO_2} of 0.27 MPa. The stable solid of Cr_2O_3 coexists with an aqueous phase $\text{Cr}(\text{OH})_3$.

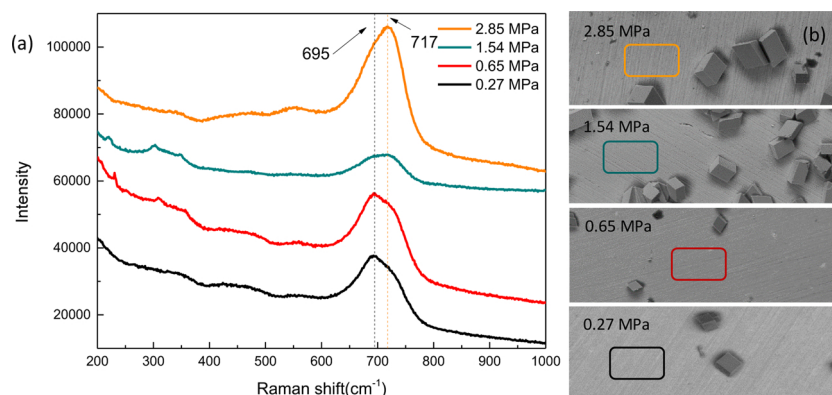


Fig. 6. The conducted local Raman scans for the corrosion products formed on 13Cr SS surface immersed in the solution at a constant temperature of 200 °C and various p_{CO_2} for 48 h.

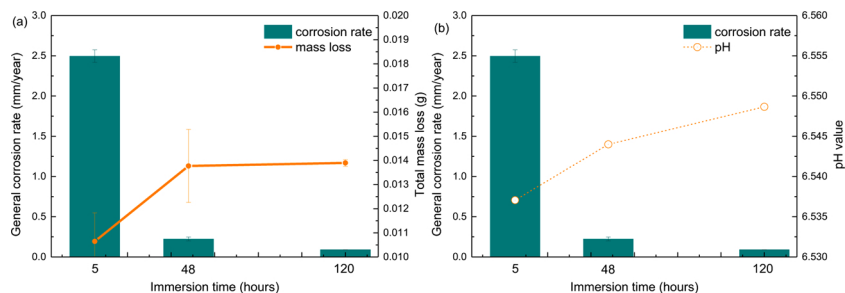


Fig. 7. The (a) corrosion rates and total mass loss of 13Cr SS, and (b) corresponding predicted bulk pH at various immersion times at 200°C and 0.27 MPa of p_{CO_2} .

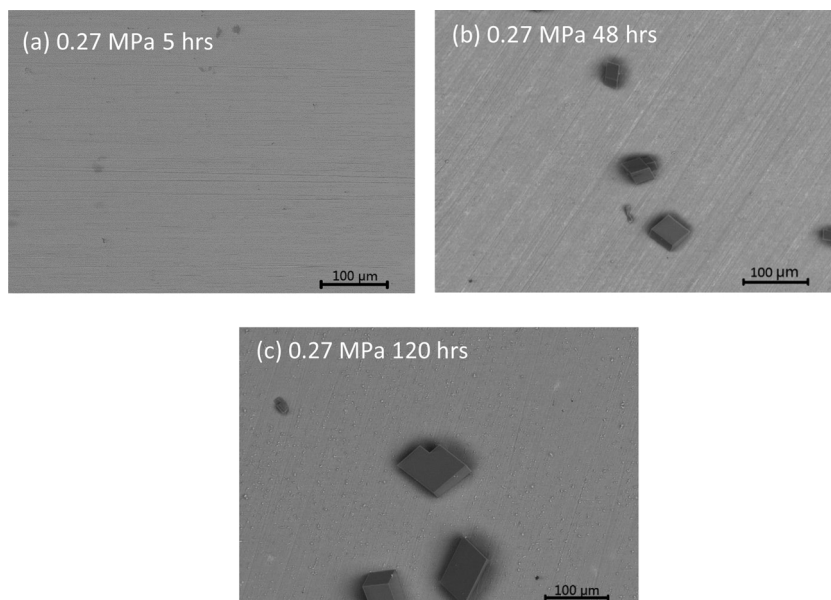


Fig. 8. Top-view SEM images of 13Cr SS immersed in the solution at 200°C and 0.27 MPa of p_{CO_2} after various durations: (a) 5 h, (b) 48 h, and (c) 120 h of exposure.

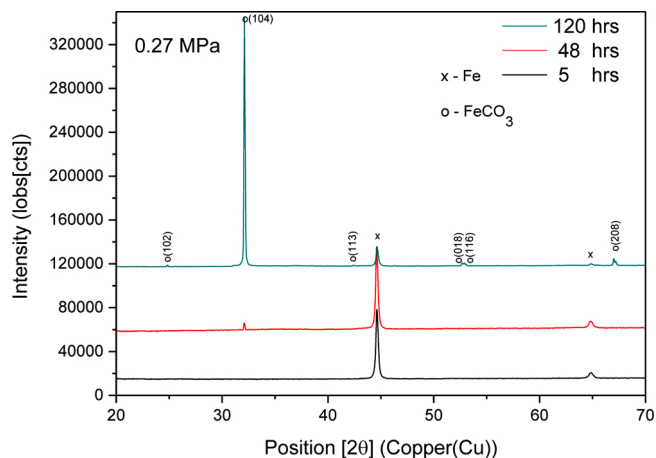
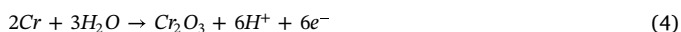
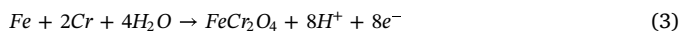


Fig. 9. XRD analysis of the 13Cr SS samples after various immersion times to the solution at 200°C and 0.27 MPa of p_{CO_2} .

Referring to the literature, the formation of Cr_2O_3 and $FeCr_2O_4$ on the surface does not follow a dissolution-precipitation process [31,40]. The formation of $FeCr_2O_4$ and Cr_2O_3 is controlled by the electro-migration process via the following anodic reactions:



During the short exposure time at 200 °C, the cathodic reaction

causes the local pH to increase due to hydrogen ion depletion. The hydrogen evolution reaction is as follows:



Meanwhile, considering the high ion activities [41] in the high temperature and pressure environment, the matrix initially dissolves to produce Fe^{2+} and Cr^{3+} on the surface at the active metal behaviour via the following reactions:



The interface pH near the metal surface decreased due to the hydrolysis reaction caused by metal ions, which subsequently influences the formation of the corrosion products, not only via an electro-migration process but also a dissolution-precipitation process such as the formation of $Cr(OH)_3$ [42]:



The precipitation of $Cr(OH)_3$ remarkably consumes the alkalinity caused by cathodic reaction and coexists with Cr_2O_3 based on the following reaction (9) [31,41]. The presence of Cr_2O_3 was confirmed by the Pourbaix diagram (as shown in Fig. 21).



In the case of 2.85 MPa p_{CO_2} (predicted pH = 5.55, corrosion potential = -0.39 V/SHE in the system), the markers are within the region where $Cr(OH)_3$ and Cr_2O_3 are stable particularly in terms of the bulk solution conditions (in Fig. 21b). The thermodynamically stable corrosion product of Fe changes from $FeCr_2O_4$ to Fe^{2+} as a reduction of pH

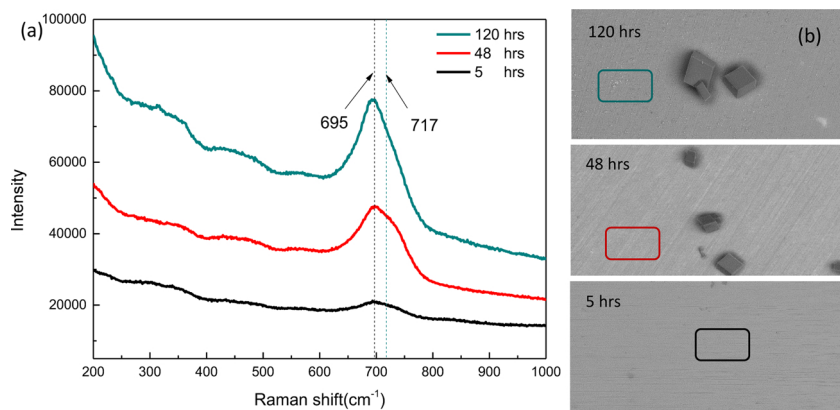


Fig. 10. Raman analysis of the 13Cr SS surfaces after various immersion times to the solution at 200°C and 0.27 MPa of p_{CO_2} .

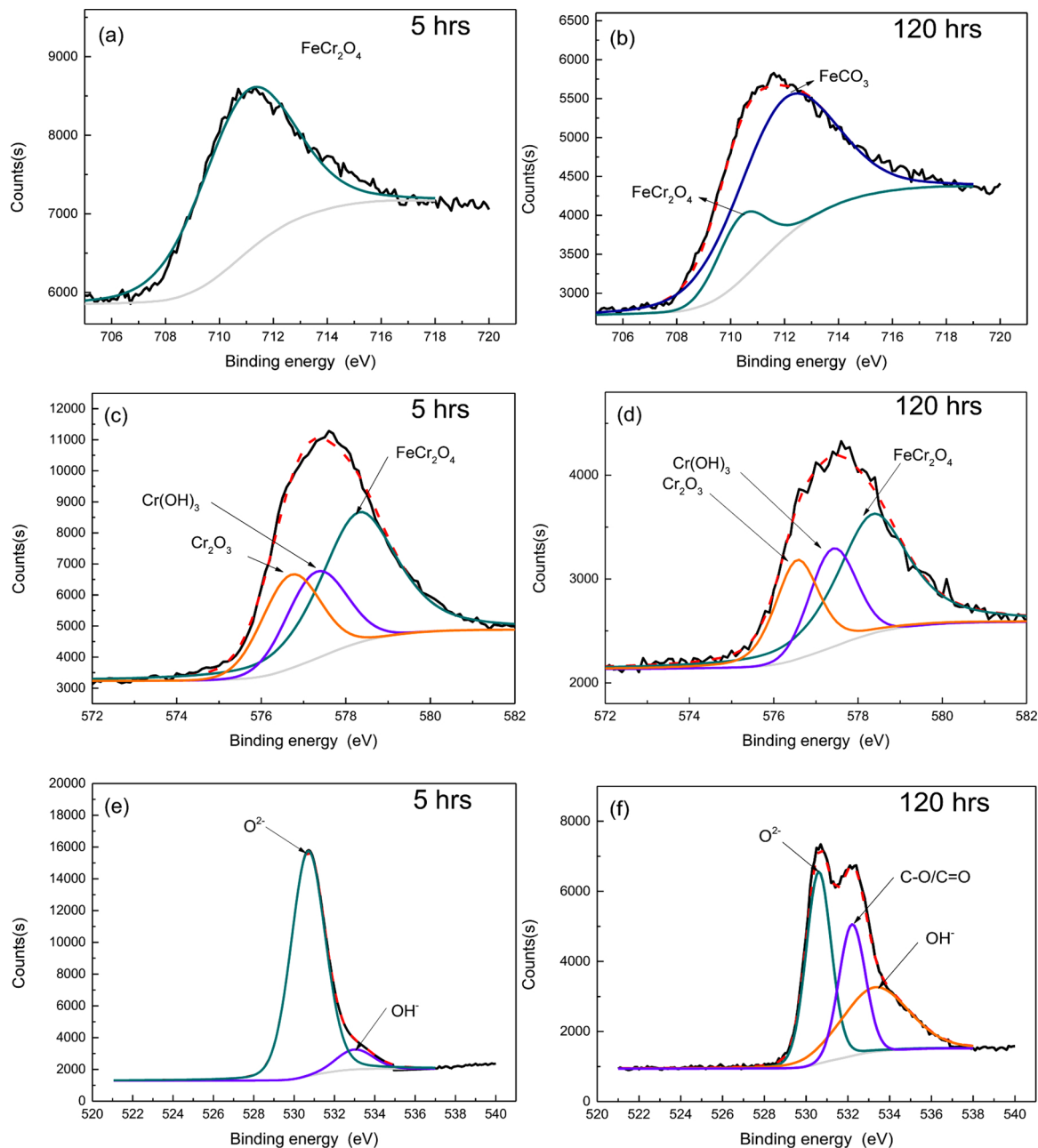


Fig. 11. XPS analysis of the 13Cr SS samples after various immersion time to the solution at 200 °C and 0.27 MPa of p_{CO_2} , (a) (b) Fe 2p_{3/2} peaks, (c) (d) Cr 2p_{3/2} peaks and (e) (f) O 1s.

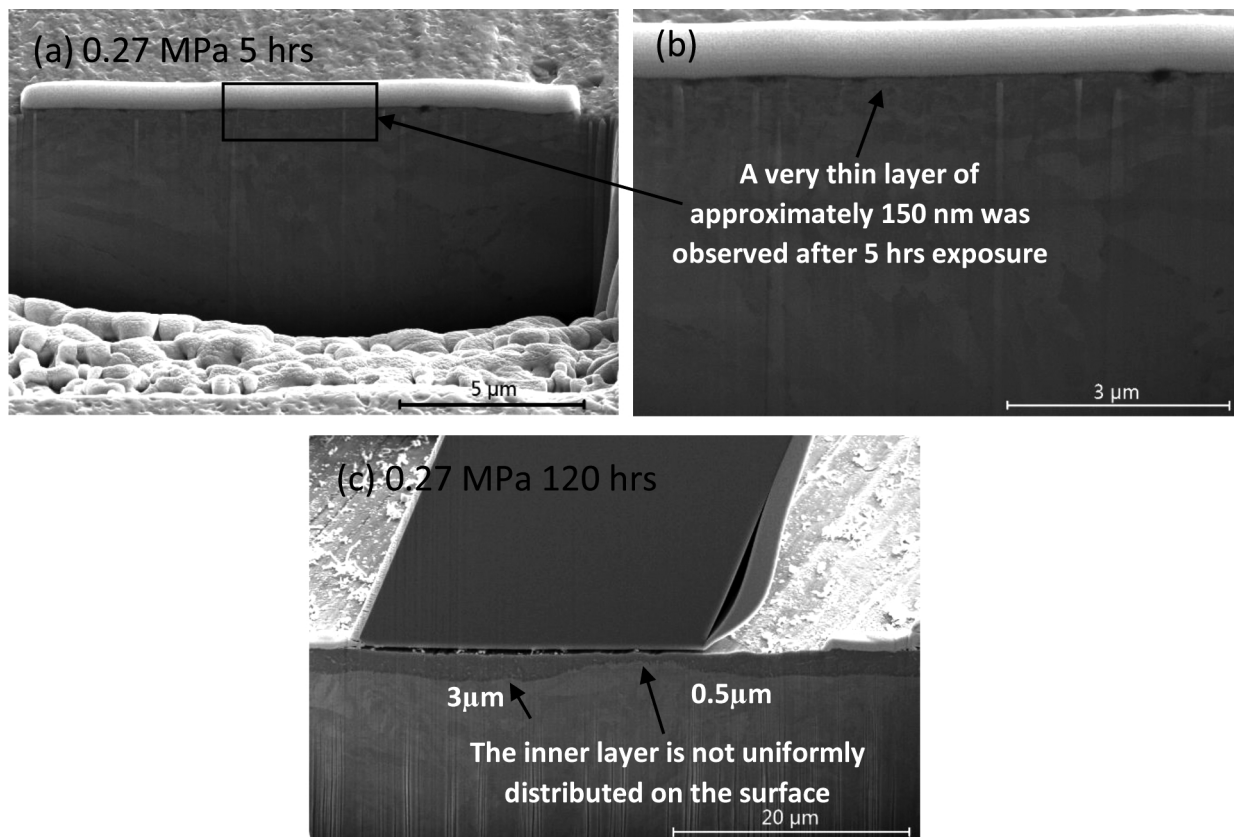


Fig. 12. Cross-sectional SEM images of 13Cr SS immersed in the solution at 200°C and 0.27 MPa of p_{CO_2} after (a) and (b) 5 h, (c) 120 h of exposure.

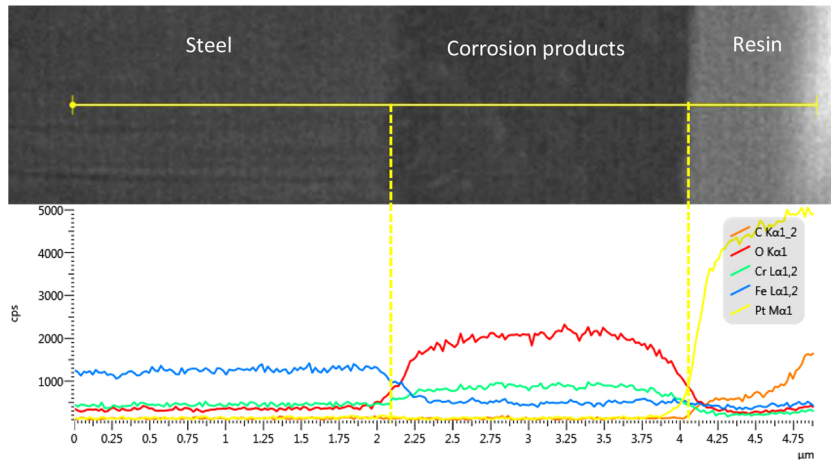


Fig. 13. EDS analyses of the 13Cr SS in the solution at 200°C and the p_{CO_2} of 0.27 MPa after 120 h of exposure.

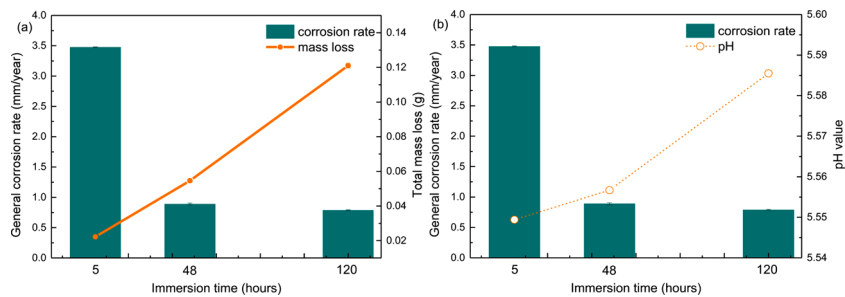


Fig. 14. Corrosion rates, total mass loss of 13Cr SS, and the corresponding predicted bulk pH at 200°C and 2.85 MPa of p_{CO_2} after various immersion durations.

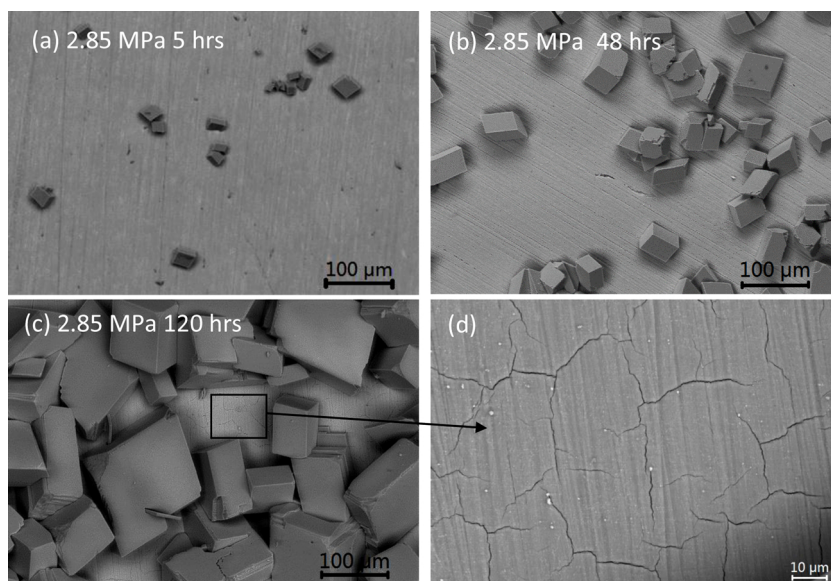


Fig. 15. Top-view SEM images of 13Cr SS exposed to the solution at 200°C and 2.85 MPa of p_{CO_2} after various durations (a) 5 h, (b) 48 h, and (c)(d) 120 h of exposure.

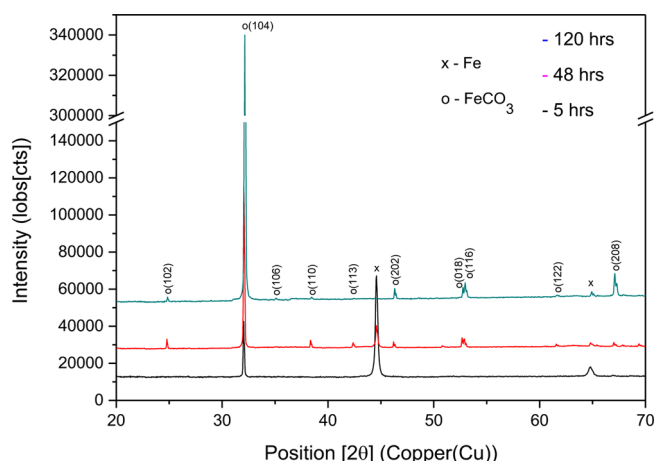


Fig. 16. XRD analysis of the 13Cr SS samples exposed to various immersion durations at 200°C and 2.85 MPa of p_{CO_2} .

value occurs. In this work, we do not consider how the Pourbaix diagram will change with the pH very close to the surface and the authors realise that this is a limitation of the work and something that is being pursued.

4.2. f Thermodynamic equilibria to understand the short-term reactions in HTHP CO_2 environments

In order to construct the Pourbaix diagram of 13Cr SS for the results within this study, the recorded mass loss after 5 h was converted to dissolved ions and used as an input to the Pourbaix diagrams in OLI calculation, the constructed Pourbaix diagrams are shown in Fig. 22. It is interesting to note that $FeCO_3$ is not presented to be stable at 0.27 MPa CO_2 after 5 h (in Fig. 22a) in contrast to 2.85 MPa CO_2 conditions (in Fig. 22b), which is in agreement with the top-view SEM images observed in Figs. 8 and 15.

The crystalline $FeCO_3$ is randomly distributed on the surface for p_{CO_2} of 2.85 MPa. The formation of $FeCO_3$ is believed to occur via the following processes:



In the CO_2 systems, previous reports suggest the growth of crystalline $FeCO_3$ due to the dissolution-precipitation processes [43]. Researchers proved that $FeCO_3$ precipitates onto the steel surface when the activities of CO_3^{2-} and Fe^{2+} ions exceed the solubility product, K_{sp} [44] (reaction 11).

In view of XRD, Raman and XPS analysis of 13Cr samples exposed to

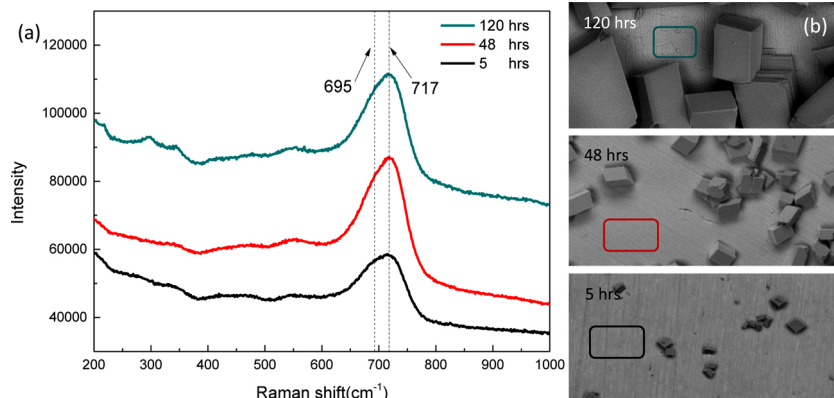


Fig. 17. Raman analysis of the 13Cr SS samples exposed to various immersion durations at 200°C and 2.85 MPa of p_{CO_2} .

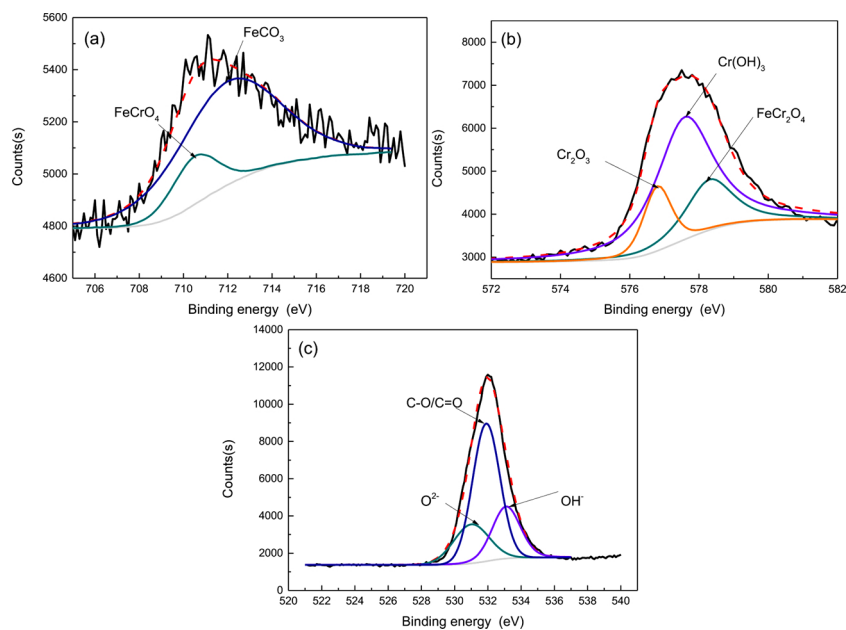


Fig. 18. XPS analysis of the 13Cr SS samples exposed to 200 °C and 2.85 MPa of p_{CO_2} after 5 h of exposure, (a) Fe 2p_{3/2} peaks, (b) Cr 2p_{3/2} peaks, and (c) O 1s.

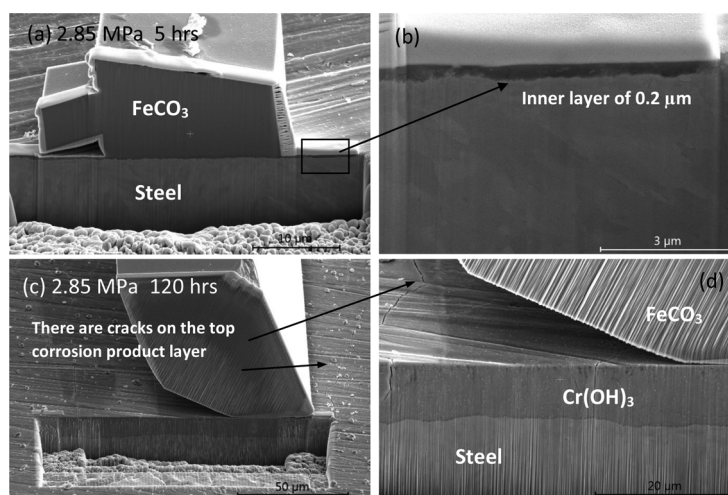


Fig. 19. Cross-section images of 13Cr SS in the solution at 200 °C and 2.85 MPa of p_{CO_2} after (a) and (b) 5 h, (c) 120 h of exposure.

the p_{CO_2} of 0.27 and 2.85 MPa for a constant temperature of 200 °C after 5 h, the corrosion products are mainly comprised of $FeCr_2O_4$, Cr_2O_3 and $Cr(OH)_3$ for 0.27 MPa p_{CO_2} and $FeCO_3$, $Cr(OH)_3$ and Cr_2O_3 for 2.85 MPa p_{CO_2} respectively. The results agree with the constructed Pourbaix diagrams for the corrosion products formed on the surface at both p_{CO_2} for short-term exposure. It can be noted that the presence of Cr_2O_3 was resulting from the undamaged pre-existing passive film on the 13Cr sample surface at 200 °C [34].

4.3. Thermodynamics to understand the long-term reactions in HTHP CO_2 environments

As time increased, the formation of the corrosion products such as the crystalline $FeCO_3$ on the surface is not only affected by the thermodynamics but also by the corrosion kinetics via dissolution-precipitation processes. $FeCO_3$ is stable at both 0.27 MPa and 2.85 MPa CO_2 conditions after 120 h as indicated in Fig. 23, which is in agreement with and confirmed by the XRD analysis as shown in Fig. 9. It is widely accepted that Pourbaix diagrams analyse the corrosion of metals based on thermodynamics. However, since the precipitation of $FeCO_3$

over the long immersion period in the solution at both 0.27 MPa and 2.85 MPa of CO_2 can be dominated by supersaturation and crystallization kinetics, the supersaturation (S) of $FeCO_3$ is important. $FeCO_3$ will precipitate as the concentration of Fe^{2+} and CO_3^{2-} ions reach the solubility limit, and the pH in the system increases during this process [45].

$$SR = \frac{[Fe^{2+}][CO_3^{2-}]}{K_{sp}} \quad (12)$$

where SR is the supersaturation of $FeCO_3$, K_{sp} is the solubility for $FeCO_3$ in mol^2/L^2 , $[Fe^{2+}]$ is the concentration of Fe^{2+} , and $[CO_3^{2-}]$ is the concentration of CO_3^{2-} . The $[Fe^{2+}]$ mainly comes from the reaction (6) and $[CO_3^{2-}]$ comes from the following dissociation reaction:



Besides, another cathodic reaction in the CO_2 system at intermediate pH ($4 < pH < 6$) would contribute to achieving supersaturation of $FeCO_3$ via enhancing HCO_3^- concentration as follows:



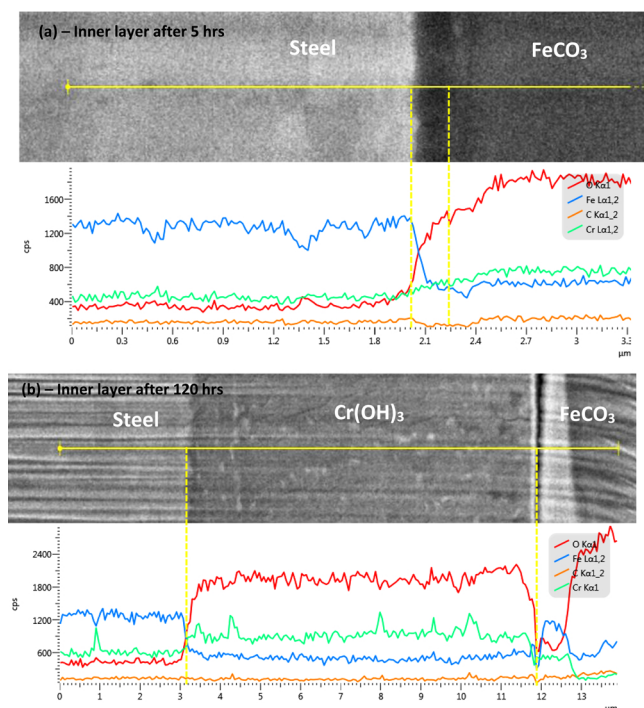


Fig. 20. EDX analyses of the 13Cr SS in the solution at 200°C and 2.85 MPa of p_{CO_2} after (a) 5 h and (b) 120 h of exposure.

From the top views of the 13Cr SS surface at 0.27 MPa p_{CO_2} as shown in Fig. 8, the number of $FeCO_3$ crystals did not increase significantly, whereas the size of the $FeCO_3$ crystals increased from 48 to 120 h. The size of $FeCO_3$ crystal growth on the 13Cr SS surface at 200 °C and p_{CO_2} of 0.27 MPa suggests low SR after 48 h of exposure as the particle growth dominates at lower levels of SR, while high SR results in a nucleation-dominating [42]. It is also suggested that the formation of the inner $FeCr_2O_4$ layer is a relatively dense barrier layer with little defects for ion transfer, which aligns with the lower corrosion rates observed as shown in Fig. 7.

Compared to the low p_{CO_2} of 0.27 MPa, $FeCO_3$ becomes thermodynamically more stable relative to $FeCr_2O_4$ for Fe base (red line) as p_{CO_2} increases to 2.85 MPa, which agrees with more precipitation of $FeCO_3$ observed from the top view SEM images (Fig. 15). The quantities of crystalline $FeCO_3$ increase with increasing p_{CO_2} , which indicates a high SR caused by high corrosion rate [42]. This effect is in a good agreement with the constructed Pourbaix diagrams, which indicate the size of the $FeCO_3$ region becomes wider as shown in Fig. 23b.

However, the $FeCO_3$ crystals tend to increase in number from 48 to 120 h at a constant p_{CO_2} of 2.85 MPa and temperature of 200 °C as shown in Fig. 15. The corrosion product kinetic observations are not fully consistent with the reported effect of long immersion times on the structure of the Pourbaix diagram as the stability of $FeCO_3$ regions are similar between 5 and 120 h in the case of high p_{CO_2} of 2.85 MPa (Figs. 22b and 23 b). It can be concluded that Pourbaix diagrams calculated the corrosion products based on the thermodynamics. However, the precipitation of $FeCO_3$ is dominated by supersaturation and

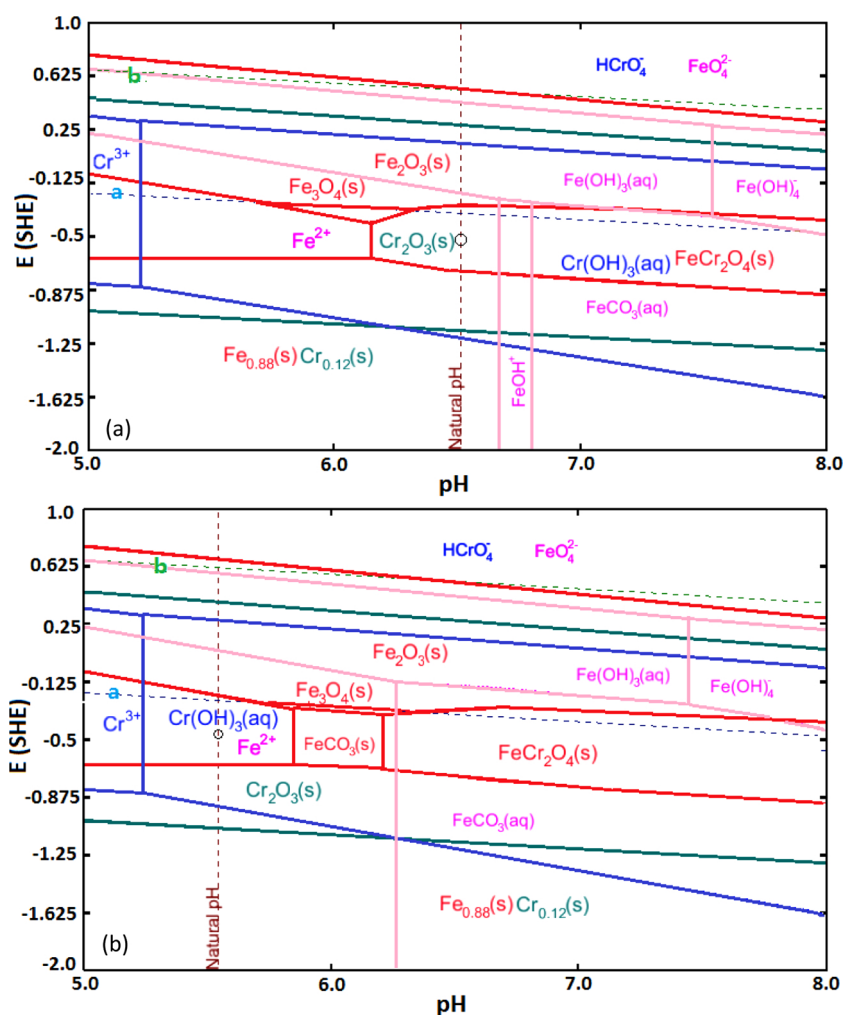


Fig. 21. Pourbaix diagram of the 13Cr SS immersed in the solution at 200°C and (a) 0.27 MPa, (b) 2.85 MPa of p_{CO_2} for less than 5 h exposure.

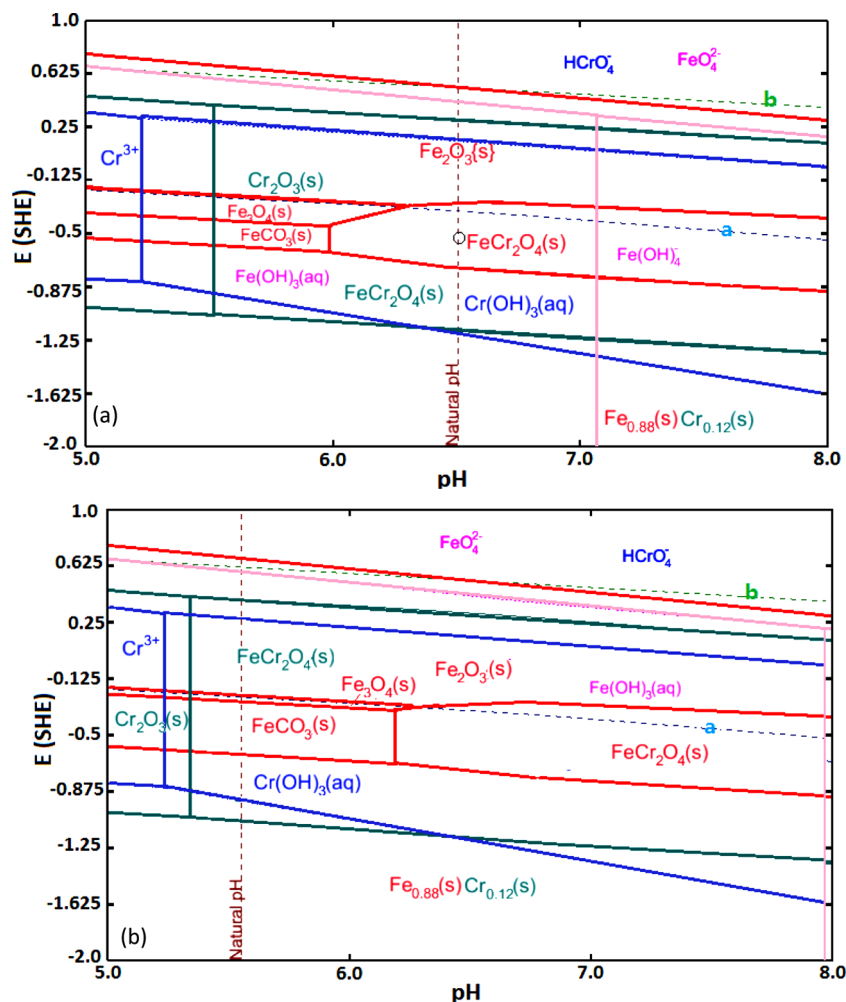


Fig. 22. Pourbaix diagram of the 13Cr SS exposed to the solution at 200°C and (a) 0.27 MPa, (b) 2.85 MPa of p_{CO_2} after 5 h.

crystallization kinetics, which is one of the limitations of only considering the Pourbaix diagrams for this system.

4.4. Capability and protectiveness of the protective corrosion products

Based on Fig. 2, an increase in the general corrosion rates is recorded as the p_{CO_2} increased which can be related to the formation of less protective properties of the corrosion products ($\text{Cr}(\text{OH})_3$ or FeCO_3 or FeCr_2O_4). The corrosion rate was low at the p_{CO_2} of 0.27 MPa, which indicates FeCr_2O_4 is able to block the active sites on the surface and has the ability to act as a diffusion barrier to protect the surface from further corrosion attack, and this results also suggest that the formation of the dense and compact FeCr_2O_4 appears to be more effective at reducing the susceptibility of the surface to general corrosion than $\text{Cr}(\text{OH})_3$ and FeCO_3 layers.

Obviously, the structure and chemical composition of the corrosion scales formed on the 13Cr SS surface depend on the p_{CO_2} which ultimately is affected due to p_{CO_2} variation in the system as well as their protective capability. The availability of H^+ for the cathodic reaction (5) increases at high p_{CO_2} conditions, decreasing the resistance to the mass transfer of H^+ and causing a higher i_{limit} . In addition to that, high p_{CO_2} of 2.85 MPa will accelerate cathodic reaction (13) which is controlled by the hydration of CO_2 , to be more corrosive [23]. From the Raman and XPS results, the main component of the layers at high pH was FeCr_2O_4 with a small amount of hydroxide ($\text{Cr}(\text{OH})_3$), while with the increase in the p_{CO_2} up to 2.85 MPa, the proportion of hydroxide increased.

An important message from this work is that the formation of the protective corrosion products varied from FeCr_2O_4 to $\text{Cr}(\text{OH})_3$ as the p_{CO_2} increased from 0.27 MPa to 2.85 MPa. The corrosion product protections to the steel surface are different, the total mass loss as shown in Fig. 14 presents the mass loss recorded for 13Cr steel at particular time instance, the increase in mass loss is higher at p_{CO_2} of 2.85 MPa than what the value has been shown in Fig. 7 for the p_{CO_2} of 0.27 MPa. For example, the total mass loss differences for 13Cr between 48 and 120 h are 0.07 g for p_{CO_2} of 2.85 MPa, from which the corrosion rate (0.72 mm/year) is shown to be high. This is in comparison to that of 13Cr steel immersed to the CO_2 -saturated solution at p_{CO_2} of 0.27 MPa, where the corrosion rate of approximately 0.01 mm/year was deduced, calculated based on the mass loss difference between 48 and 120 h. Therefore, this thick $\text{Cr}(\text{OH})_3$ layer formed on the surface at p_{CO_2} of 2.85 MPa provides poor corrosion resistance compared to the thin FeCr_2O_4 layer observed in the experiments of lower p_{CO_2} of 0.27 MPa.

Fig. 24 illustrates the schematic diagrams of the film formation process under both p_{CO_2} at various immersion times. The formation of the corrosion product films at high p_{CO_2} of 2.85 MPa mainly composed hydroxide and this layer is thicker and more uniform. However, the matrix covering by FeCr_2O_4 is a non-uniform layer at the lower p_{CO_2} of 0.27 MPa. The formation of the corrosion products on super 13Cr at the lower p_{CO_2} of 0.27 MPa including three stages: Stage I, the local passive film breakdown; Stage II, the growth of FeCr_2O_4 dominated inner layer and starting precipitation of crystalline FeCO_3 ; Stage III, the development of the inner FeCr_2O_4 layer and growth of the outer crystalline FeCO_3 size. For the p_{CO_2} of 2.85 MPa, the corrosion scales also evolved

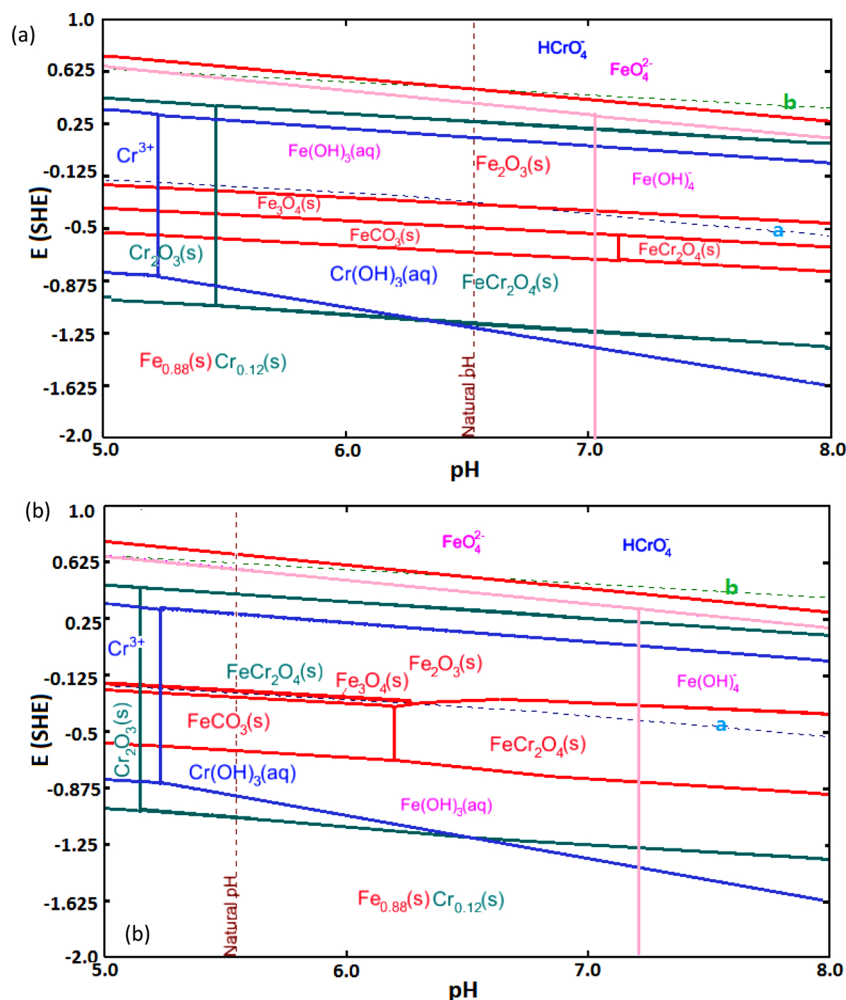


Fig. 23. Pourbaix diagram of the 13Cr SS exposed to the solution at 200°C and (a) 0.27 MPa, (b) 2.85 MPa of p_{CO_2} after 120 h.

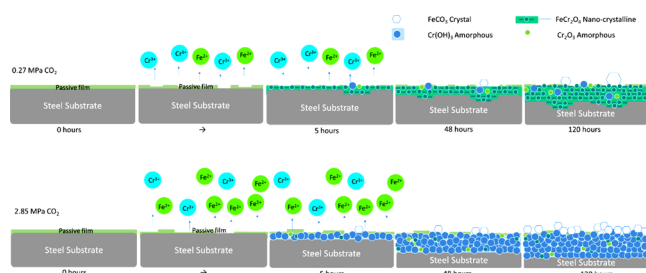


Fig. 24. The formation and evolution of the films on the 13Cr SS surface at 200°C and various p_{CO_2} .

in three stages: Stage I, the local dissolution of the passive film; Stage II, the precipitation of $Cr(OH)_3$ -dominated inner layer and the outer crystalline $FeCO_3$; Stage III, the thickness of the inner $Cr(OH)_3$ layer increased as well as the increase in crystalline $FeCO_3$ number.

However, one of the important issues was drawn is the change in brine chemistry by using a closed vessel cell such as autoclaves and the consequences this has on the development of the corrosion products on the surface was fast as well as the corrosion rate reduced due to the protective corrosion products formed on the surface. At 200 °C, the concentration of Fe^{2+} and CO_3^{2-} ions reach the solubility limit fast, resulted in the increase the bulk pH in the system (it is important to note that the surface pH is not the same to the bulk pH within the system), followed by the precipitation of $FeCO_3$ on the surface. This is

the one that needs to be careful in the static experiments and the production of metal ions and consumption of H^+ at the material interface are fast, resulting in accelerating the corrosion processes or the corrosion product precipitation occurred at the material interface, reducing the corrosion rate in a short period. Future study to address this issue are needed regarding the brine renewing in laboratory conditions, in order to better understand the protectiveness of the developed corrosion products on the 13Cr surface.

5. Conclusions

The characteristics of the corrosion product scales and corrosion behaviour of 13Cr steel in a CO_2 -saturated solution at 200 °C have been investigated at various p_{CO_2} respectively within this study. The study focused on the corrosion product kinetics and the evolution of corrosion product scales on the surface. The following main conclusions could be made:

- 1 The corrosion scales formed on 13Cr at 200 °C varied with p_{CO_2} : when the p_{CO_2} was below 0.65 MPa, the primary composition of the corrosion scales was $FeCr_2O_4$; as the p_{CO_2} beyond 1.54 MPa, the presence of $Cr(OH)_3$ and $FeCO_3$ crystals observed on the surface.
- 2 The inner corrosion product layer formed at 200 °C and p_{CO_2} of 0.27 MPa is mainly containing $FeCr_2O_4$. The thickness of the $FeCr_2O_4$ layer is non-uniform distributed on the surface but shows excellent corrosion resistance to the surface. The outer layer is confirmed as $FeCO_3$. The $FeCO_3$ crystals are randomly distributed and not increasing in number over 120 h of immersion time. However, the size

of the FeCO_3 crystals increased significantly with immersion time prolong.

- 3 For the condition of p_{CO_2} of 2.85 MPa, the corrosion products also display the double-layered structure comprising of inner and outer layers. The inner corrosion product layer mainly was $\text{Cr}(\text{OH})_3$ and uniformly covered the entire surface coexists underneath the FeCO_3 crystal. However, this film shows the poor ability against cations transfer, indicating its structure with a high density of defects. The out layer is confirmed as FeCO_3 crystals.

Authors statement

Category 1

Conception and design of the study: Xiaoqi Yue, Yong Hua.

Acquisition of data: Xiaoqi Yue, Yong Hua.

Analysis and/or interpretation of data: Xiaoqi Yue, Yong Hua.

Category 2

Drafting the manuscript: Xiaoqi Yue, Yong Hua, Lei Zhang, Chong Sun, Shesheng Xu, Anne Neville, Minxu Lu, Chun Wang.

Revising the manuscript critically for important intellectual content: Xiaoqi Yue, Yong Hua, Lei Zhang, Chong Sun, Shesheng Xu, Anne Neville, Minxu Lu, Chun Wang.

Category 3

Approval of the version of the manuscript to be published (the names of all authors must be listed): Xiaoqi Yue, Yong Hua, Lei Zhang, Minxu Lu, Anne Neville, Chong Sun, Shesheng Xu, Chun Wang.

Declaration of Competing Interest

None.

Acknowledgements

This work has received funding from the European Research Council (ERC) under the European Union's Horizon 2020 research and innovation programme (Grant agreement No. 742930). We would like to thank Mr. John Harrington, Dr Zabeada Aslam and Mr. Stuart Micklethwaite from the University of Leeds, Electron Microscopy and Spectroscopy Centre (LEMAS) for the assistance with FIB measurements.

References

- N. Baddoo, Stainless steel in construction: a review of research, applications, challenges and opportunities, *J. Constr. Steel Res.* 64 (2008) 1199–1206.
- N. Baddoo, 100 years of stainless steel: a review of structural applications and the development of design rules, *SESOJ* 26 (2013) 17.
- R. Klueh, Elevated temperature ferritic and martensitic steels and their application to future nuclear reactors, *Int. Mater. Rev.* 50 (2005) 287–310.
- A. Turnbull, A. Griffiths, Corrosion and cracking of weldable 13 wt-% Cr martensitic stainless steels for application in the oil and gas industry, *Corros. Eng. Sci. Technol.* 38 (2003) 21–50.
- M. Kimura, Y. Miyata, K. Sakata, R. Mochizuki, Corrosion resistance of martensitic stainless steel OCTG in high-temperature and high CO_2 environment, *Corros.* 2004, NACE International, 2004.
- S. Marcelin, N. Pèbère, S. Régnier, Electrochemical characterisation of a martensitic stainless steel in a neutral chloride solution, *Electrochimica Acta.* 87 (2013) 32–40.
- Z. Dai, H. Viswanathan, R. Middleton, F. Pan, W. Ampomah, C. Yang, W. Jia, T. Xiao, S.-Y. Lee, B. McPherson, others, CO_2 accounting and risk analysis for CO_2 sequestration at enhanced oil recovery sites, *Environ. Sci. Technol.* 50 (2016) 7546–7554.
- Y. Hua, S. Xu, Y. Wang, W. Taleb, J. Sun, L. Zhang, R. Barker, A. Neville, The formation of FeCO_3 and Fe_3O_4 on carbon steel and their protective capabilities against CO_2 corrosion at elevated temperature and pressure, *Corros. Sci.* 157 (2019) 392–405.
- P. Li, Y. Zhao, B. Liu, G. Zeng, T. Zhang, D. Xu, H. Gu, T. Gu, F. Wang, Experimental testing and numerical simulation to analyze the corrosion failures of single well pipelines in Tahe oilfield, *Eng. Fail. Anal.* 80 (2017) 112–122.
- W. Qi, J. Wang, X. Li, Y. Cui, Y. Zhao, J. Xie, G. Zeng, Q. Gao, T. Zhang, F. Wang, Effect of oxide scale on corrosion behavior of HP-13Cr stainless steel during well completion process, *J. Mater. Sci. Technol.* (2019), <https://doi.org/10.1016/j.jmst.2019.10.009> in press.
- P. Felton, M.J. Schofield, Understanding the high temperature corrosion behavior of modified 13%Cr martensitic OCTG, *Anal. Chim. Acta.* 58 (1998) 470–472.
- J. Enerhaug, P.E. Kvaale, M. Bjordal, J.M. Drugli, T. Rogne, Qualification of welded super 13% Cr martensitic stainless steels for the Sgard field, *Corros.* 99, NACE International, 1999.
- Y. Hua, R. Jonnalagadda, L. Zhang, A. Neville, R. Barker, Assessment of general and localized corrosion behavior of X65 and 13Cr steels in water-saturated supercritical CO_2 environments with SO_2/O_2 , *Int. J. Greenh. Gas Control.* 64 (2017) 126–136.
- T.J. Mesquita, E. Chauveau, M. Mantel, N. Bouvier, D. Koschel, Corrosion and metallurgical investigation of two supermartensitic stainless steels for oil and gas environments, *Corros. Sci.* 81 (2014) 152–161.
- H. Marchebois, H.E. ALAMI, J. Leyer, A. Gateaud, others, Sour service limits of 13% Cr and super 13% Cr stainless steels for OCTG: effect of environmental factors, *Corros.* 2009, NACE International, 2009.
- M. Al-Saeedi, D. Al-Enezi, M. Sounderrajan, A. Saxena, G. Gumballi, D. McKinnell, others, First implementation of CRA casing in sour HPHT reservoirs in deep wells in Kuwait, North Afr. Tech. Conf. Exhib. Society of Petroleum Engineers, 2013.
- N. Sridhar, R. Thodla, F. Gui, L. Cao, A. Anderko, Corrosion-resistant alloy testing and selection for oil and gas production, *Corros. Eng. Sci. Technol.* 53 (2018) 75–89.
- Y. Hua, A. Shamsa, R. Barker, A. Neville, Protectiveness, morphology and composition of corrosion products formed on carbon steel in the presence of Cl^- , Ca^{2+} and Mg^{2+} in high pressure CO_2 environments, *Appl. Surf. Sci.* 455 (2018) 667–682.
- S. Guo, L. Xu, L. Zhang, W. Chang, M. Lu, Characterization of corrosion scale formed on 3Cr steel in CO_2 -saturated formation water, *Corros. Sci.* 110 (2016) 123–133.
- X. Yue, M. Zhao, L. Zhang, H. Zhang, D. Li, M. Lu, Correlation between electrochemical properties and stress corrosion cracking of super 13Cr under an HTHP CO_2 environment, *RSC Adv.* 8 (2018) 24679–24689.
- A. Ikeda, S. Mukai, M. Ueda, Corrosion behavior of 9 to 25% Cr steels in wet CO_2 environments, *Corrosion* 41 (1985) 185–192.
- A. Pfennig, R. Wiegand, M. Wolf, C.-P. Bork, Corrosion and corrosion fatigue of AISI 420C (X46Cr13) at 60°C in CO_2 -saturated artificial geothermal brine, *Corros. Sci.* 68 (2013) 134–143.
- S. Nestic, J. Postlethwaite, S. Olsen, An electrochemical model for prediction of corrosion of mild steel in aqueous carbon dioxide solutions, *Corrosion* 52 (1996) 280–294.
- J. Crolet, N. Thevenot, S. Nestic, Role of conductive corrosion products in the protectiveness of corrosion layers, *Corrosion* 54 (1998) 194–203.
- Y. Zhao, W. Qi, J. Xie, Y. Chen, T. Zhang, D. Xu, F. Wang, Investigation of the failure mechanism of the TG-201 inhibitor: promoting the synergistic effect of HP-13Cr stainless steel during the well completion, *Corros. Sci.* (2020) 108448.
- L. Mu, W. Zhao, Investigation on carbon dioxide corrosion behaviour of HP13Cr110 stainless steel in simulated stratum water, *Corros. Sci.* 52 (2010) 82–89.
- R. Moreira, C. Franco, C. Joia, S. Giordana, O. Mattos, The effects of temperature and hydrodynamics on the CO_2 corrosion of 13Cr and 13Cr5Ni2Mo stainless steels in the presence of free acetic acid, *Corros. Sci.* 46 (2004) 2987–3003.
- X. Lei, Y. Peng, A. Fu, J. Zhang, Z. Bai, C. Yin, C. Lu, Investigation of stress corrosion cracking behavior of super 13Cr tubing by full-scale tubular goods corrosion test system, *Eng. Fail. Anal.* 50 (2015) 62–70.
- H. Zhang, Y. Zhao, Z. Jiang, Effects of temperature on the corrosion behavior of 13Cr martensitic stainless steel during exposure to CO_2 and Cl^- environment, *Mater. Lett.* 59 (2005) 3370–3374.
- X. Li, Y. Zhao, W. Qi, J. Xie, J. Wang, B. Liu, G. Zeng, T. Zhang, F. Wang, Effect of extremely aggressive environment on the nature of corrosion scales of HP-13Cr stainless steel, *Appl. Surf. Sci.* 469 (2019) 146–161.
- Y. Zhao, X. Li, C. Zhang, T. Zhang, J. Xie, G. Zeng, D. Xu, F. Wang, Investigation of the rotation speed on corrosion behavior of HP-13Cr stainless steel in the extremely aggressive oilfield environment by using the rotating cage test, *Corros. Sci.* 145 (2018) 307–319.
- OLI system, n.d.
- A.C.G.-1 on C. of Metals, Standard Practice for Preparing, Cleaning, and Evaluating Corrosion Test Specimens, ASTM international, 2011.
- X. Yue, L. Zhang, Y. Wang, S. Xu, C. Wang, M. Lu, A. Neville, Y. Hua, Evolution and characterization of the film formed on super 13Cr stainless steel in CO_2 -saturated formation water at high temperature, *Corros. Sci.* (2019) 108277.
- L. Xu, B. Wang, J. Zhu, W. Li, Z. Zheng, Effect of Cr content on the corrosion performance of low-Cr alloy steel in a CO_2 environment, *Appl. Surf. Sci.* 379 (2016) 39–46.
- J. Langevoort, I. Sutherland, L. Hanekamp, P. Gellings, On the oxide formation on stainless steels AISI 304 and incoloy 800H investigated with XPS, *Appl. Surf. Sci.* 28 (1987) 167–179.
- M.C. Biesinger, B.P. Payne, A.P. Grosvenor, L.W. Lau, A.R. Gerson, R.S.C. Smart, Resolving surface chemical states in XPS analysis of first row transition metals, oxides and hydroxides: Cr, Mn, Fe, Co and Ni, *Appl. Surf. Sci.* 257 (2011) 2717–2730.
- M. Biesinger, C. Brown, J. Mycroft, R. Davidson, N. McIntyre, X-ray photoelectron spectroscopy studies of chromium compounds, *Surf. Interface Anal. Int. J. Devoted Dev. Appl. Tech. Anal. Surf. Interfaces Thin Films* 36 (2004) 1550–1563.
- D. Radziuk, L. Mikhnavets, M. Vorokhta, V. Matolín, L. Tabulina, V. Labunov, Sonochemical formation of copper/iron-modified graphene oxide nanocomposites for ketorolac delivery, *Chem. Eur. J.* 25 (2019) 6233–6245.
- V. Trindade, U. Krupp, P.E.-G. Wagenhuber, H.-J. Christ, Oxidation mechanisms of Cr-containing steels and Ni-base alloys at high-temperatures— Part I: the different role of alloy grain boundaries, *Mater. Corros.* 56 (2005) 785–790.
- Y. Zhao, J. Xie, G. Zeng, T. Zhang, D. Xu, F. Wang, Pourbaix diagram for HP-13Cr

- stainless steel in the aggressive oilfield environment characterized by high temperature, high CO₂ partial pressure and high salinity, *Electrochimica Acta* 293 (2019) 116–127.
- [42] S. Guo, L. Xu, L. Zhang, W. Chang, M. Lu, Corrosion of alloy steels containing 2% chromium in CO₂ environments, *Corros. Sci.* 63 (2012) 246–258.
- [43] M.H. Sk, A.M. Abdullah, M. Ko, B. Ingham, N. Laycock, R. Arul, D.E. Williams, Local supersaturation and the growth of protective scales during CO₂ corrosion of steel: effect of pH and solution flow, *Corros. Sci.* 126 (2017) 26–36.
- [44] A. Dugstad, Fundamental aspects of CO₂ metal loss corrosion-part 1: mechanism, *Corros.* 2006, (2006).
- [45] E. Van Hunnik, B.F. Pots, E. Hendriksen, The Formation of Protective FeCO₃ Corrosion Product Layers in CO₂ Corrosion, NACE International, Houston, TX (United States), 1996 Paper No. 6.
- [46] Yang Zhao, Shuyun Cao, Tao Zhang, Junfeng Xie, Dake Xu, Fuhui Wang, A new high-efficiency experimental design for optimizing various flow velocities testing in extremely aggressive formation water, *Acta Metall. Sinica* 32 (2019) 944–950.